



# Suppression of winter heavy precipitation in Southeastern China by the Kuroshio warm current

Guangzhi Xu<sup>1</sup> · Ping Chang<sup>1</sup> · Xiaohui Ma<sup>1</sup> · Mingkui Li<sup>1</sup>

Received: 16 January 2019 / Accepted: 21 June 2019 / Published online: 25 June 2019  
© The Author(s) 2019

## Abstract

The possible effects of the Kuroshio current and associated sea surface temperature (SST) fronts on Southeastern China winter precipitation are examined using twin simulations of a regional atmospheric model. When the SST frontal features in the forcing data are artificially weakened, the simulated rainfall over Southeastern China, particularly heavy rainfall, is found to increase by a statistically significant amount, compared to the simulations with the observed SST fronts. This difference is attributed to an anomalous regional overturning circulation that interferes with the onshore moisture transport. With the presence of stronger frontal SSTs, an anomalous ascending motion is anchored along the warm current, with a descending branch to its western side, forming a circulation cell that strides across the coasts of Southern China. In days of heavy rainfall over the Southeastern China, the regional atmospheric circulation tunnels oceanic moisture onto land across the coasts, serving as the primary water vapor source for the precipitation. This process is weakened by the anomalous regional overturning circulation in that the imbalance between low-level offshore and upper-level onshore flux drains the land of moisture, and the up-lifted moisture import aloft creates unfavorable condition for land precipitation.

**Keywords** SST front · Precipitation · Kuroshio current

## 1 Introduction

Although precipitation in Southern China is typically muted in winter (defined here as November–March) relative to spring or summer, extreme rainfall events (some in the form of ice storm or wet-freezing) can lead to considerable damages and losses in transportation (Xie et al. 2014), power supply (Ye 2014), human health (Zhou et al. 2014), biomass (Zhou et al. 2017) and are among the most costly and disruptive winter weather hazards in Southeastern China (Zhou et al. 2011; Deng et al. 2012; Ren and Ren 2017).

From a climate dynamics point of view, the Southern China winter precipitation characteristics are closely related

with various climatic modes that have land and/or ocean origins, including the Madden-Julian Oscillation (MJO) (e.g. Jia et al. 2011; Yao et al. 2015), El Niño–Southern Oscillation (ENSO) (Wang et al. 2000; Wu et al. 2003; Zhou and Wu 2010), East Asia Winter Monsoon (EAWM) (Compo et al. 1999; Wu and Chan 1997; Zhou and Wu 2010; Zhou 2011), the dynamic and thermodynamic processes related to the Tibetan Plateau (Wan and Wu 2007), European blocking (Huang et al. 2018b) and as will be discussed later, regional atmospheric circulations. The realism of Southern China rainfall simulations can therefore serve as a surrogate metric for the physical understanding as well as model skills in regard to the above mentioned drivers and their interactions. Besides, the atmosphere in this season has some unique features that distinguish it from other seasons, such as a northward shifted and intensified Hadley cell (Oort and Yienger 1996), the prevailing land-to-ocean low-level winds associated with winter Monsoon (Cai et al. 2017), larger MJO strengths (Jia et al. 2011) and stronger temperature gradients across air-sea interface, making the winter precipitation an important topic to investigate.

Sea surface temperature (SST) and its contrast with land surface temperature are among the most important factors in

---

**Electronic supplementary material** The online version of this article (<https://doi.org/10.1007/s00382-019-04873-3>) contains supplementary material, which is available to authorized users.

---

✉ Guangzhi Xu  
xugzhi1987@gmail.com

<sup>1</sup> Key Laboratory of Physical Oceanography, Institute for Advanced Ocean Studies, Ocean University of China and Qingdao National Laboratory for Marine Science and Technology, Qingdao, China

modulating land precipitation. Li et al. (2016) documented a negative relationship between the long-term trends in spring time Southern China rainfall and South China Sea and the Philippine Sea SST, and highlighted the importance of tropical SSTs and regional convective circulation. At basin scales, the warming trend over the Pacific warm pool region has been associated with a drying trend over South Asia in boreal summer (Annamalai et al. 2013), while the trend of the tropical Indian ocean has been found to contribute to a winter wetting in mid-eastern China (Li et al. 2015). At regional scales, the role of meso-scale, frontal SST features in affecting Southern China rainfall may also be important, but has not been carefully considered. Given that the western boundary current systems, including the Kuroshio, are hot spots in the global ocean where the fastest warming trends are observed (Wu et al. 2012), it is important to examine the potential role of SST fronts in modulating regional rainfall.

The importance of meso-scale SSTs in large scale atmospheric circulation and rainfall variability has received increasing attentions in the recent decade, thanks to availability of high-resolution observations and numerical models. It has been shown that frontal SSTs along the western boundary warm currents, such as the Kuroshio and Gulf Stream, can remotely affect the position of mid-latitude storm tracks (Brayshaw et al. 2008; Small et al. 2014; Ma et al. 2015, 2017).

There is also abundant evidence that meso-scale SSTs induced by ocean fronts can locally affect the overlying winds, giving rise to persistent atmospheric divergence/convergence observable from high-resolution satellite radar scatterometry (Pan et al. 2002; Chelton et al. 2004) and reproducible using atmospheric model with sufficiently high resolution forced by high resolution SSTs (e.g. Ma et al. 2017). The along-front wind convergence is shown to produce a deep convective structure, penetrating beyond the planetary boundary layer into the free atmosphere, accompanied by an anchored rain belt, increased occurrences of low Out-going Long-wave Radiation (OLR) and high clouds (Pan et al. 2002; Minobe et al. 2008; Xu et al. 2011). More evidences of the atmospheric responses to frontal Kuroshio SSTs are provided by Xie et al. (2001), Liu et al. (2013), with the associated low-cloud morphology effects further examined by Liu et al. (2016). With increased air-sea temperature gradients occurring in the cold season, the SST front induced wind convergence reaches its peak intensity in winter and spring (Pan et al. 2002; Liu et al. 2013, 2016). However, the effects also exist in summer and has been found to have a considerable enhancement effect on local, oceanic precipitation in analyses of reanalysis, satellite and modelling experiments (Sasaki et al. 2012; Sasaki and Yamada 2018). Very recently, Liu et al. (2018) also show a robust rainfall response to ocean eddies over major oceanic frontal zones, such as the Kuroshio Extension (KE).

However, discussions on precipitation responses in the above mentioned studies are all confined to the front regions over ocean, the possible impacts beyond local scale to nearby land surfaces have been largely absent.

With the increasing evidence pointing to the role of frontal SSTs in atmospheric variability, this study intends to fill a gap in our understanding of winter heavy precipitation events over Southern China and their relationship to frontal SSTs in the neighboring marginal seas. Using a set of twin high-resolution regional atmospheric model simulations we will explore differences in terrestrial rainfall distribution with and without the presence of meso-scale SST features. This work is an extension of earlier studies by Ma et al. (2015, 2017) with a focus on local atmospheric responses.

This paper is organized as follows. Section 2 introduces the data and model experiment design. Section 3 presents the results of the twin experiments with a particular focus on winter heavy rainfall and the associated moisture convergence, moisture flux vertical profile and circulation differences that lead to a proposed mechanism relating SST fronts in the neighboring marginal seas to rainfall. Section 4 gives a summary to the findings and a discussion in a broader context.

## 2 Methods and data

The Weather Research and Forecasting (WRF) model was used to carry out the numerical experiments. The model domain covers the eastern China and North Pacific ( $3.6^{\circ}$  N– $66^{\circ}$  N,  $99^{\circ}$  E– $270^{\circ}$  E), and has a horizontal resolution of 27 km, sufficiently fine to capture meso-scale SST effects on the atmosphere (Ma et al. 2017). Identical initial and boundary conditions from the NCEP2 reanalysis (Kanamitsu et al. 2002) are used for the control (Ctrl) and filter (Filt) experiments, with the former being forced by the  $0.09^{\circ}$  ( $\sim 10$  km) Microwave InfraRed Optimal Interpolated (MW-IR) SST from the Remote Sensing Systems ([www.remss.com](http://www.remss.com)), and the later by a spatially low-pass filtered MW-IR SST. Using a  $15^{\circ}$  (*longitude*)  $\times$   $5^{\circ}$  (*latitude*) cut-off wavelength, the Loess filter halves the spectral power of the meso-scale SST variability with length scales less than  $\sim 800$  km in the observed SST dataset, while preserving the large scale SST variance. More details on the SST smoothing and the model configurations can be found in Ma et al. (2015, 2017), and snapshots of Ctrl, Filt and Ctrl-Filt SST difference are provided in the supplementary figure S1. The seasonal average SST gradient differences between Ctrl and Filt is shown in Fig. S1d, with magnitudes confined within observational range (Sasaki and Yamada 2018).

Both Ctrl and Filt experiments are carried out for 13 boreal winter seasons (initialized on October-1, integrated to March-31 of the next year) from 2002/3 to 2014/5, each

with two ensemble members. Provided that each pair of Ctrl-Filt experiments share identical lateral boundaries and initial conditions, this sample size should provide a sufficiently large data basis to establish the statistical confidence of analyses as we demonstrate below. The Tropical Rainfall Measuring Mission (TRMM) 3B42 observation (Tropical Rainfall Measuring Mission (TRMM) 2011) during the same time period is used as an observational reference for precipitation comparisons. “Heavy rainfall” is defined as daily rain rates above the 75 % percentile in the respective dataset (Ctrl, Filt and TRMM.) Daily averages of various WRF variables are used unless otherwise stated, and necessary details of analysis methods will be supplemented as needed upon introduction of results.

In examining the relationship between the precipitation and the divergence of horizontal moisture fluxes timeseries, we used the information flow in linear dynamic systems as a measure of the causality relationship, on top of their correlations (Liang 2014). For a pair of timeseries  $X_1$  and  $X_2$ , the rate of information flowing (in nats per unit time) from the latter to the former is given as

$$T_{2 \rightarrow 1} = \frac{C_{11}C_{12}C_{2,d1} - C_{12}^2C_{1,d1}}{C_{11}^2C_{22} - C_{11}C_{12}^2} \tag{1}$$

where  $C_{ij}$  is the sample covariance between  $X_i$  and  $X_j$ ,  $C_{i,dj}$  is the covariance between  $X_i$  and  $\dot{X}_j$ , and  $\dot{X}_j$  the difference approximation of  $\frac{dX_j}{dt}$  using the Euler forward scheme:

$$\dot{X}_{j,n} = \frac{X_{j,n+1} - X_{j,n}}{\Delta t} \tag{2}$$

A positive  $T_{2 \rightarrow 1}$  signals a driving force from  $X_2$  to  $X_1$ , while a negative value indicates that  $X_2$  tends to stabilize  $X_1$ . Applications of information flow have been shown to provide some valuable insights on the interactions between ENSO and the Indian Ocean Dipole (IOD) mode (Liang 2014).

### 3 Results

#### 3.1 Southeastern China rainfall distribution

Comparison with TRMM observation illustrates that the WRF simulations captured reasonably well the major patterns of average (Fig. 1a, c) and heavy precipitation (Fig. 1b, d) over China and the Northwest Pacific (NWP) in winter, although in both cases the WRF model tends to overestimate, particularly over an diagonal band covering mid-eastern China, the Bohai Sea and the Sea of Japan in the heavy rainfall category (Fig. 1f). Like with other seasons, there exists a well-defined north–south contrast in heavy rainfall amounts, with the region south of the

Yangtze river and east of the Tibetan plateau being wetter than the rest of the country. We define this region loosely as the Southeastern China (SEC) region. A technical definition of SEC for various computational purposes can be found in Fig. 1b. WRF overestimation in SEC is also relatively low, at about 1–3 mm/day for the seasonal mean, and 3–5 mm/day for the 75% percentile.

#### 3.2 Southeastern China rainfall difference

Figure 2a reveals some notable differences in the heavy rainfall distribution with the observed and weakened frontal SST forcing. A narrow band of positive anomalies is found in Ctrl, extending from the South China Sea northward across the East China Sea, and splitting into two branches at the southern tip of Kyushu. One branch enters the Sea of Japan via the Tsushima straight, and the other grazes the southern side of Japan into the KE region. Parallel with the band of positive rainfall anomalies are two flanks of dry anomalies on each side. The western flank covers the SEC region with larger values near the coast (Fig. 2a). Seasonal mean difference in heavy rainfall over SEC goes up to  $\sim -2.7$  mm/day, with a regional average of  $\langle \delta P \rangle = -0.86$  mm/day. Differences in the seasonal mean overall rainfall (not shown) share nearly identical patterns with the heavy rainfall subset but with reduced magnitudes, suggesting a considerable contribution from the latter. Also note that the region of SEC collocate with region of complex topography (not shown), where topographic effect plays an important role in creating rainfall, particularly heavy rainfall.

The histograms of SEC rainfall in Fig. 2b substantiate this argument. Typical Gamma-like precipitation distribution is shown with high skewness on the heavy rain rate (right) tail. A Ctrl deficit is observed in all bins of rain rates greater than  $\sim 1$  mm/day, but becomes larger towards the heavy rain tail, starting roughly from the Ctrl and Filt combined 75% percentile at 12.9 mm/day. The rightmost pair of bins compares the seasonal accumulations in Ctrl and Filt measured in (m), and suggests a total difference of  $-0.95$  m, of which about 67% comes from differences above the 75% percentile. A Kernel Density Estimate (KDE) analysis (Wilks 2011) is performed using a Gaussian kernel with 2 mm/day bandwidth, to remove possible effects from arbitrary bin edge choices. The resultant curves of KDE confirm that the rainfall differences between Ctrl and Filt in the seasonal average is mainly attributed to decreased heavy rainfall. Overestimate of WRF simulations with respect to TRMM is also revealed in the PDFs, and is likely attributable to the Kain-Fritsch convection scheme used in the model (Ma et al. 2017).

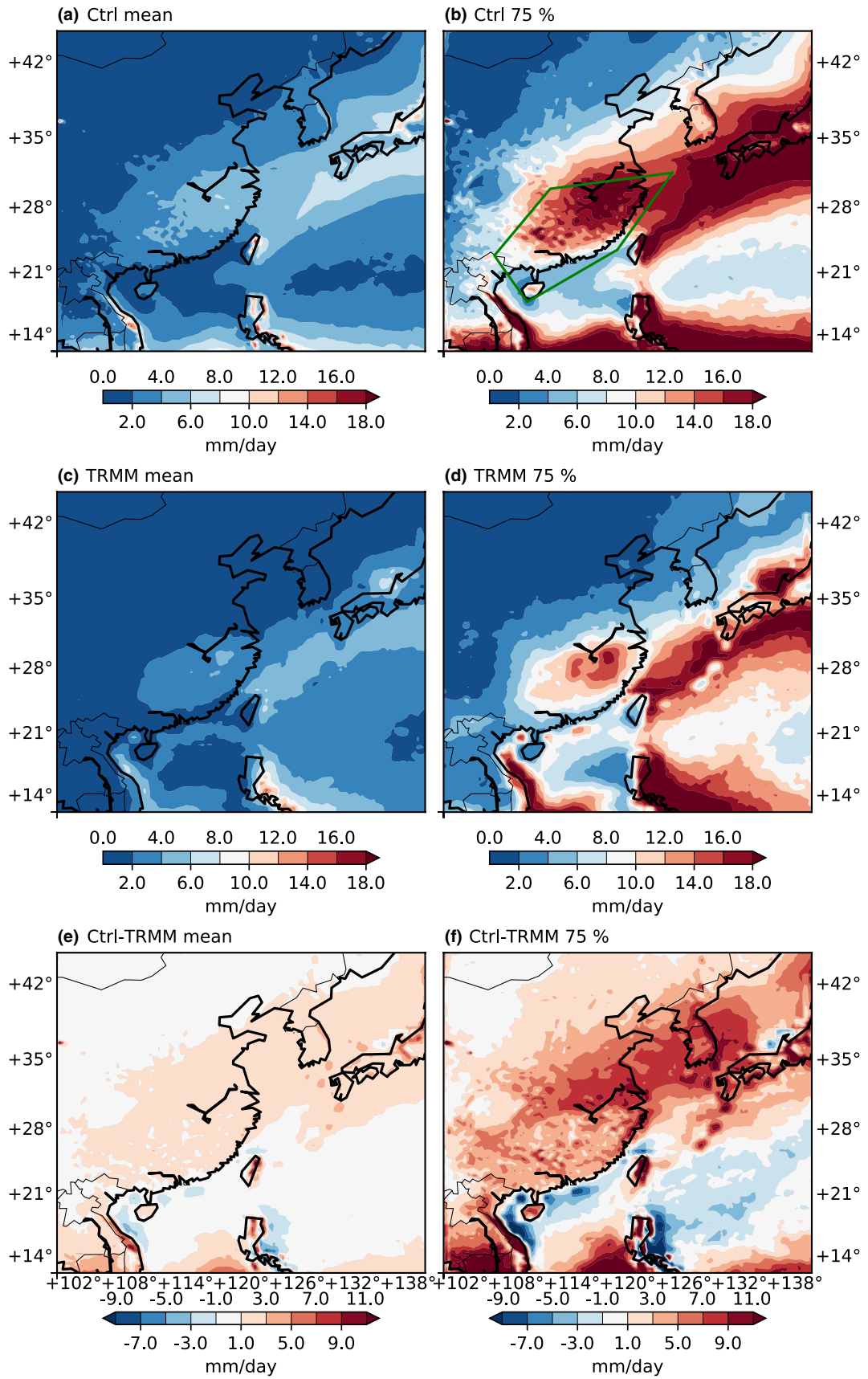


**Fig. 1** Seasonal mean and heavy rainfall (in mm/day) distributions in Ctrl (top panel), TRMM observation (mid panel) and the Ctrl-TRMM differences (bottom panel). Left column shows the seasonal mean (mean of 2002/03–2014/15). Right column shows the heavy rainfall, defined as daily rain rates greater than the 75% percentile in the respective dataset. A green pentagon is drawn to denote the technical definition of SEC region (excluding ocean grids), and will be used throughout of this work

### 3.3 Anomalous regional overturning circulation

These rainfall anomalies shown above have close correspondences with frontal SST anomalies (Fig. 3a): the wet anomalies in the East China Sea and Kuroshio Extension area co-locate with the western boundary warm current of the NWP and its extension, and the Sea of Japan wet anomaly is associated with the Tsushima warm current, which has been found to have impacts on regional rainfall (e.g. Hirose and Ki 2006; Iizuka 2010; Sato and Sugimoto 2013; Ogata and Kitoh 2014).

In response to the anomalous SST distribution, vertical wind velocity difference between Ctrl and Filt show a negative (upward) anomaly along the warm current in the lower troposphere (Fig. 3b). Similar pattern has been found along the Gulf Stream warm current (Minobe et al. 2008; Kobashi et al. 2008; Liu et al. 2016; Sasaki et al. 2012; Xu et al. 2011). Frontal SST anomalies induce low level pressure adjustments and wind convergence/divergence on the cold/warm flanks of the warm current (Xie 2004; Chelton et al. 2004; Minobe et al. 2008). While in the Filt experiment, such effects are largely weakened by the reduced frontal SST forcing. This boundary layer effect has rather deep penetration into the free troposphere. Figure 3c shows the cross-front vertical profile of Ctrl-Filt difference in vertical wind velocity averaged during heavy rainfall days. Observed is a narrow band of anomalous upward flow centered along the warm current extending into the mid-troposphere. Accompanied with this strong ascending motion is the anomalous rain band shown in Fig. 2a, and corresponding to the descending motion are the two precipitation deficit bands sandwiching the warm current. Below  $\sim 700$  hPa the differences in vertical velocity also show consistent differences in horizontal wind divergences: an anomalous divergence zone is found on top of a surface convergence zone along the warm current, and the reversed pattern is found in the descending flanks, the western of which is responsible for the SEC rainfall deficit. This descending branch itself does not have a great spatial coverage, however, as will be demonstrated later, it inhibits onshore moisture transport and renders a precipitation response to a greater spatial extent over land.

Note that Filt shows a slight warming near the coast of SEC, as shown in Fig. 3a, which could provide a more favourable condition for evaporation and potentially contribute to the terrestrial precipitation enhancement. However,

this near-coast evaporation enhancement in Filt is overshadowed by the enhancement over the warm current itself in Ctrl, consistent with previous findings (Xu et al. 2011). A comparison (not shown) of the total column water content in Ctrl and Filt during heavy rainfall days shows that although surface latent heat flux has a close match with SST difference, where Filt shows warmer coastal SST along the coast of southeast China, the vapor load difference does not show a close match with the SST difference along the coast, except off the coast of Fujian, east of Taiwan, where there is an increase of the vapor load, consistent with the stronger latent heat flux in the Filt. Therefore, it is possible that the warmer SST in this region may make a contribution to the enhanced heavy rainfall in Filt. However, the moisture transport analysis indicates that the onshore transport difference is mainly determined by the change in circulation rather than vapor load itself. Therefore, we believe that the overall effect of this near-coastal warmer SST enhanced evaporation in Filt is no match to that due to the evaporation enhancement over the warm current in Ctrl, and the regional overturning circulation anchored by warm current in Ctrl exerts a much larger impact on the re-distribution of vapor than that determined by the local near coast evaporation enhancement in Filt. When it comes to precipitation over land, horizontal moisture divergence/convergence is a much stronger factor than local evaporation.

### 3.4 Relation with atmospheric moisture divergence

The scarcity of winter rainfall in China is mainly due to the prevailing low level land-to-ocean monsoonal wind that constantly replenish the dry and cold air mass in the atmosphere (Cai et al. 2017; Huang et al. 2018a). Precipitation events in this season are mostly associated with synoptic frontal systems, for instance marching cold surges that create disturbances and upward motion, providing dynamic conditions for precipitation to occur. Modest to heavy precipitation systems usually draw in precipitable water more from converged or transported moisture than from local evaporation. The moisture collecting radius of rainfall-producing systems can be 3–5 times the radius of actual precipitating area (Trenberth et al. 2003). The relative importance of local evaporation with respect to atmospheric convergence (i.e. moisture recycling) is quite different over oceanic, flux-rich regions (e.g. warm current and KE), than over land surfaces (Trenberth et al. 2007). In the case of winter SEC rainfall, one should expect an even lower moisture recycling contribution, given the cold land surface at this time of year. Huang et al. (2018a) estimated that about 67% of the moisture for winter season extreme precipitation events in southern China has oceanic origins. Given the above, we expect a close correspondence between SEC rainfall and atmospheric moisture convergences.

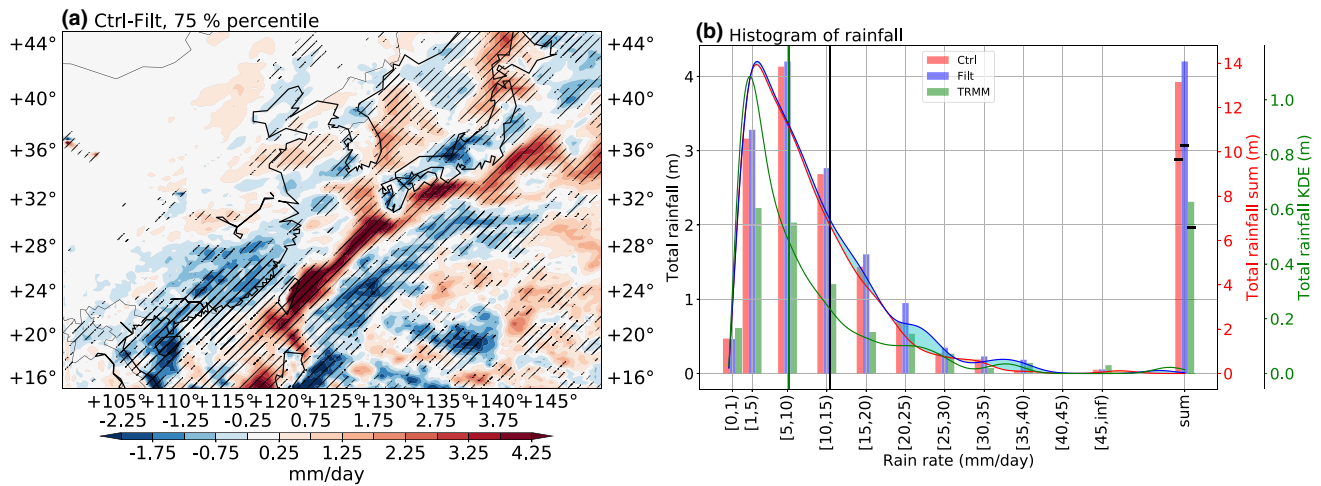


**Fig. 2** **a** Average Ctrl-Filt difference in heavy rainfall in mm/day, hatching indicates differences being significant at  $p \leq 0.05$  level, according to a 2-tailed Wilcoxon–Mann–Whitney (WMW) rank test. Daily ensemble values are concatenated rather than averaged to avoid inter-ensemble cancellations, giving a dof of  $0.75 \times 13 \text{ years} \times 151 \text{ days} \times 2 \text{ ensembles} - 1 = 981$ . **b** Histograms of daily rainfall in Ctrl (red), Filt (blue) and TRMM (green). The right-most bin shows the total rainfall (in m, plotted onto the red y-axis

on the right). The red, blue and green curves are the Kernel Density Estimate (KDE) of the respective distribution, using a Gaussian kernel with 2 mm/day bandwidth. The KDE curves are plotted onto the green y-axis on the right, and the cyan shading shows the Ctrl deficits. The vertical black line denotes the rain rate at 75% percentile in WRF simulations, the vertical green line denotes the rain rate at 75% percentile in TRMM. The black horizontal bars denote the rainfall accumulations above the 75% percentile, in respective dataset

Results displayed in Fig. 4 substantiate this claim. Figure 4a shows the timeseries of Ctrl-Filt differences of area-averaged SEC precipitation (blue) and divergence of column moisture fluxes (red), both subject to a 31-day moving average. Vertical integration of moisture flux is first computed using

$$Q = \int_{p_1}^{p_2} \frac{Vq}{g} dp \tag{3}$$

where  $V$ ,  $q$  and  $p$  are horizontal wind, specific humidity and pressure, respectively.  $p_1$  and  $p_2$  are 100 and 1000 hPa, respectively. Care has been taken to account for the extra layer between surface and  $p_2$ , and pressure layers that are beneath the surface. Then the horizontal divergence is computed as

$$D = \frac{\partial Q_u}{\partial x} + \frac{\partial Q_v}{\partial y} \tag{4}$$

and scaled to the unit of mm/day.

It can be seen in Fig. 4a that the close negative correlation and comparable amplitudes between the two timeseries suggest a strong control of moisture divergences over precipitation. The correlation between the non-smoothed precipitation and divergence in Ctrl (Ctrl-Filt difference) is  $-0.49$  ( $-0.53$ ), both being significant according to Student’s t test. Timeseries are sub-sampled

by every 10 days before correlation computation to remove possible effects from auto-correlation (Trenberth 1984).

Spatially, moisture divergences that show significant (negative) correlation with SEC mean precipitation cover the SEC region itself and extend northeastward into the NWP (Fig. 4b). This diagonal pattern is likely the combined effect from southeastward marching cold fronts (Yao et al. 2015; Wu and Chan 1997) and the northward moisture transport during heavy rainfall periods (Huang et al. (2018a, b), Jia and Ge (2017), more on this later). Precipitation composites created from surge events (defined by tracking strong 850 hPa level geopotential height anomalies) reveal similar diagonal structure (not shown). Therefore this can be regarded as a characteristic large scale rainfall distribution pattern for winter SEC.

When it comes to the Ctrl-Filt difference, this region narrows down to a better fit to the SEC area, with some positive correlations found to the east of Taiwan (Fig. 4c). Going one step further from correlation to causality, we computed the information flow in linear dynamic systems. According to Liang (2014), a positive information flow from moisture divergence to precipitation ( $T(\delta D \rightarrow \delta P >))$  implies a driving causality relationship on top of their (negative) correlation (Fig. 4d). The same statistics computed on SEC averaged moisture divergence and SEC precipitation ( $T(< D > \rightarrow < P >))$  in Ctrl is  $0.25 \pm 0.01$  (labelled in Fig. 4a), and in the Ctrl-Filt counter-parts

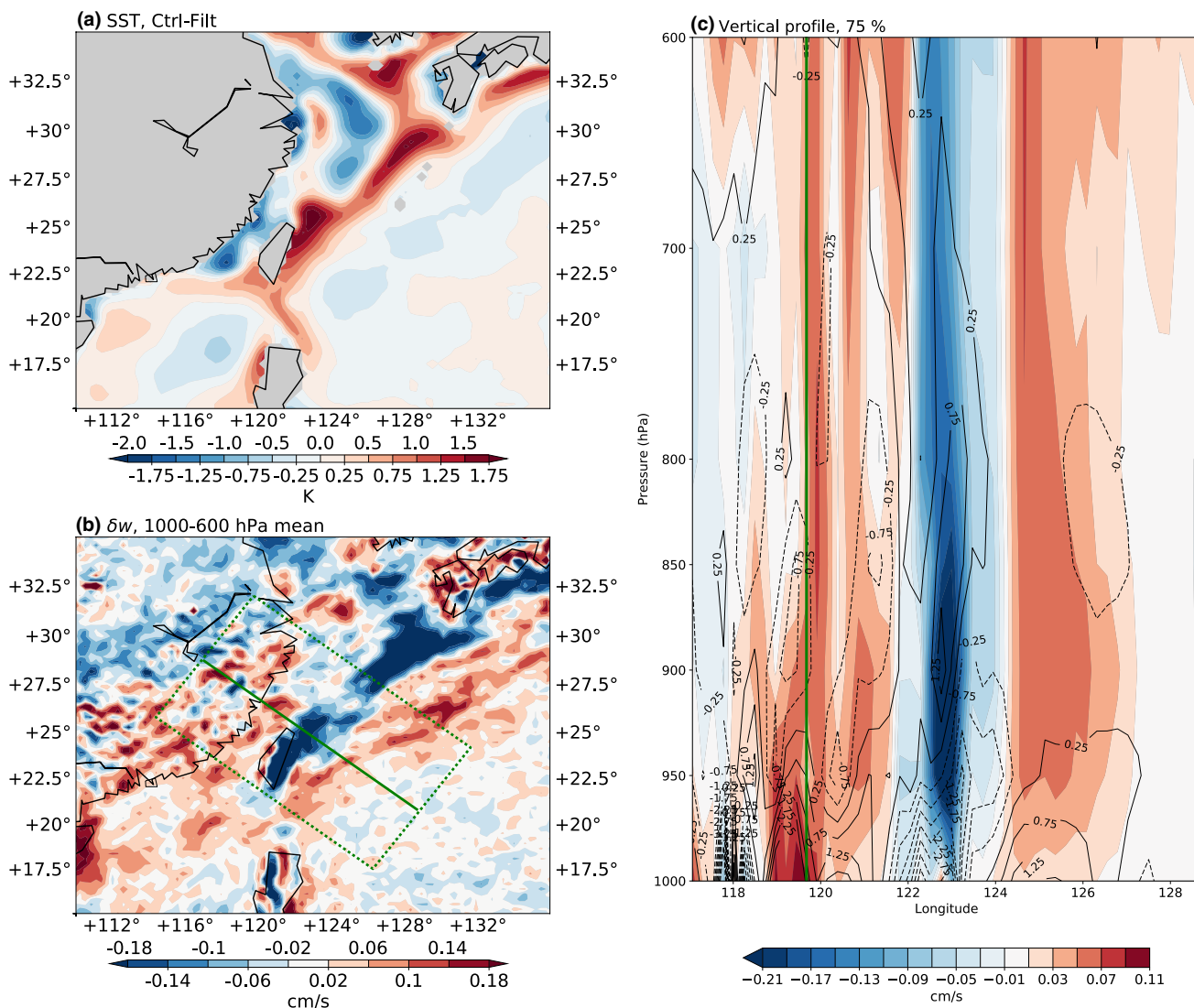


**Fig. 3** **a** Average Ctrl-Filt difference in SST, in K. **b** Ctrl-Filt difference in vertical wind velocity, averaged between 1000 and 600 hPa during heavy rainfall days, in cm/s. **c** vertical profile of average Ctrl-Filt vertical wind velocity difference during heavy rainfall days, shown as colors in cm/s. The corresponding horizontal wind

divergence difference is shown as contours, with an interval of  $0.5 \times 10^{-6} \text{ s}^{-1}$ , and the negative contours are plotted in dash. The profiles are obtained by averaging data in the green dashed region shown in **b**, along the solid green line. The vertical green line denotes the *approximate* land-sea boundary

$(T(\langle \delta D \rangle \rightarrow \langle \delta P \rangle))$  is  $0.34 \pm 0.02$ . Therefore moisture converged in the atmosphere serves as the primary water source for SEC precipitation.

### 3.5 Vertical distribution of cross boundary moisture fluxes

Having established the association between SEC precipitation and atmospheric moisture convergence, we next give a more detailed depiction of the moisture transport into SEC. By converting the areal integral of moisture convergences to the contour integral of inward fluxes around its boundaries, moisture transport from different directions

can be examined and their relative importance evaluated. Boundary grid cells of the SEC region was obtained by subtracting the binary erosion (Gonzalez and Woods 2001) (with a  $3 \times 3$  diamond structuring element) from its original mask. Net input flow is computed as the summed products of boundary grid box lateral span ( $dx$  and  $dy$ ) and the moisture flux in the normal direction ( $Q_v$  and  $Q_u$ , respectively). The average of two adjacent grid cells is used as the cross-boundary flux, and the normal direction is defined as inward pointing being positive, therefore a closed contour integral approximates the total convergence of moisture fluxes. The SEC boundary is divided into three sections: Section 1 ( $\widehat{CA}$  in Fig. 5a) as the western

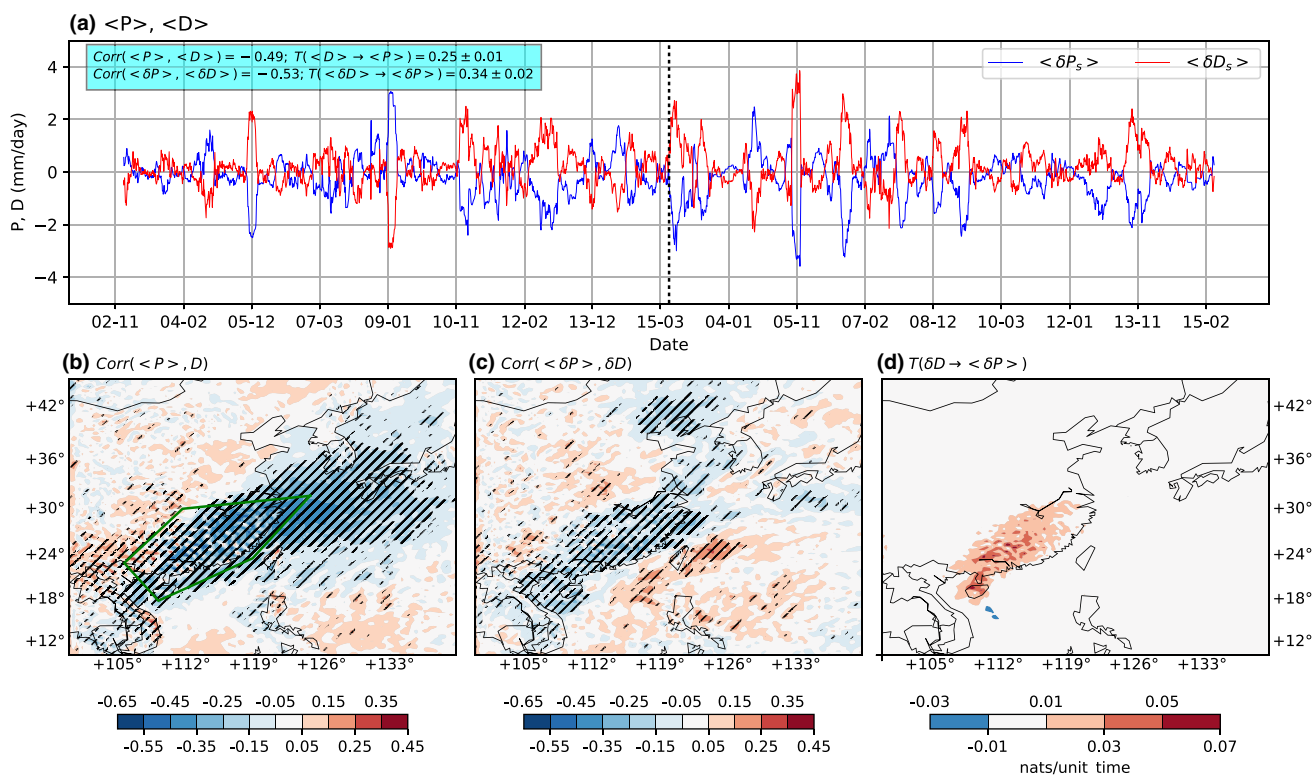


**Fig. 4** **a** Time series of Ctrl-Filt differences in SEC precipitation ( $\langle \delta P_s \rangle$ , blue) and divergence of vertically integrated moisture fluxes ( $\langle \delta D_s \rangle$ , red). Both timeseries are in mm/day and are smoothed using a 31-day moving average. Vertical black dashed line denotes where the two ensemble members are concatenated. Correlation coefficients between moisture divergence and SEC precipitation, and the information flow using non-smoothed timeseries are labelled at top left corner. **b** Spatial distribution of correlation coefficients

between SEC precipitation and moisture divergences in Ctrl. Hatching indicates correlation being significant at  $p \leq 0.01$  level according to Student's t test. Green pentagon defines the SEC region as in Fig. 1b. **c** Similar as **b** but for Ctrl-Filt differences. Correlations in **a–c** are computed on 10-day sub-sampled timeseries, to counter possible artifacts from auto-correlation. **d** Information flow from the Ctrl-Filt moisture divergence difference to the SEC precipitation difference, in nats/unit time

boundary, Section 2 ( $\widehat{AB}$ ) the northern boundary, and Section 3 ( $BDC$ ) the coastal boundary.

Figure 5a shows the mean vertically integrated moisture fluxes during heavy rainfall days, and Fig. 5c gives a panoramic view of the vertical profile, starting from and finishing at the start of Section 1. It should be noted that although the transport of moisture is mostly southwesterly over SEC, the vertical integration seems to hide an important 2-layer vertical structure: a lower layer that is confined to the boundary layer (below  $\sim 800$  hPa), bringing in moisture from the East China Sea and South China Sea across the coastal Section 3 boundary (Fig. 5c), and an upper southwesterly layer that imports moisture originated from the North Indian Ocean and Southeast Asia across Section 1, above  $\sim 800$  hPa level (Fig. 5c). Although humidity load drops with height, higher westerly wind speed and greater air column thickness renders the upper southwesterlies taking over in the integrated result.

However, much of the upper layer input across Section 1 is then exported at roughly the same height at the northern part of Section 3, starting from the Yangtz River delta down to the coasts of Fujian (Fig. 5a, c). Although this does not necessarily imply that moisture from the western boundary makes no contribution to precipitation, the temporal correlation of the SEC precipitation with the Section 1 net input is indeed lower than with the Section 3 input (0.23 vs. 0.36 for 10-day sub-sampled daily timeseries; 0.28 vs. 0.45 for monthly). Using a Lagrangian back-tracking method, Huang et al. (2018a) estimated moisture sources for winter time extreme precipitations over South China, and showed that the South China Sea and East China Sea sources constitute a much greater contribution (exceeding 1.5 mm/day) than the Southeast Asia source (up to 0.4 mm/day). Furthermore, moisture originated from multiple source locations including the South China Sea, East China Sea, and NWP all tend to follow a similar vector into SEC through

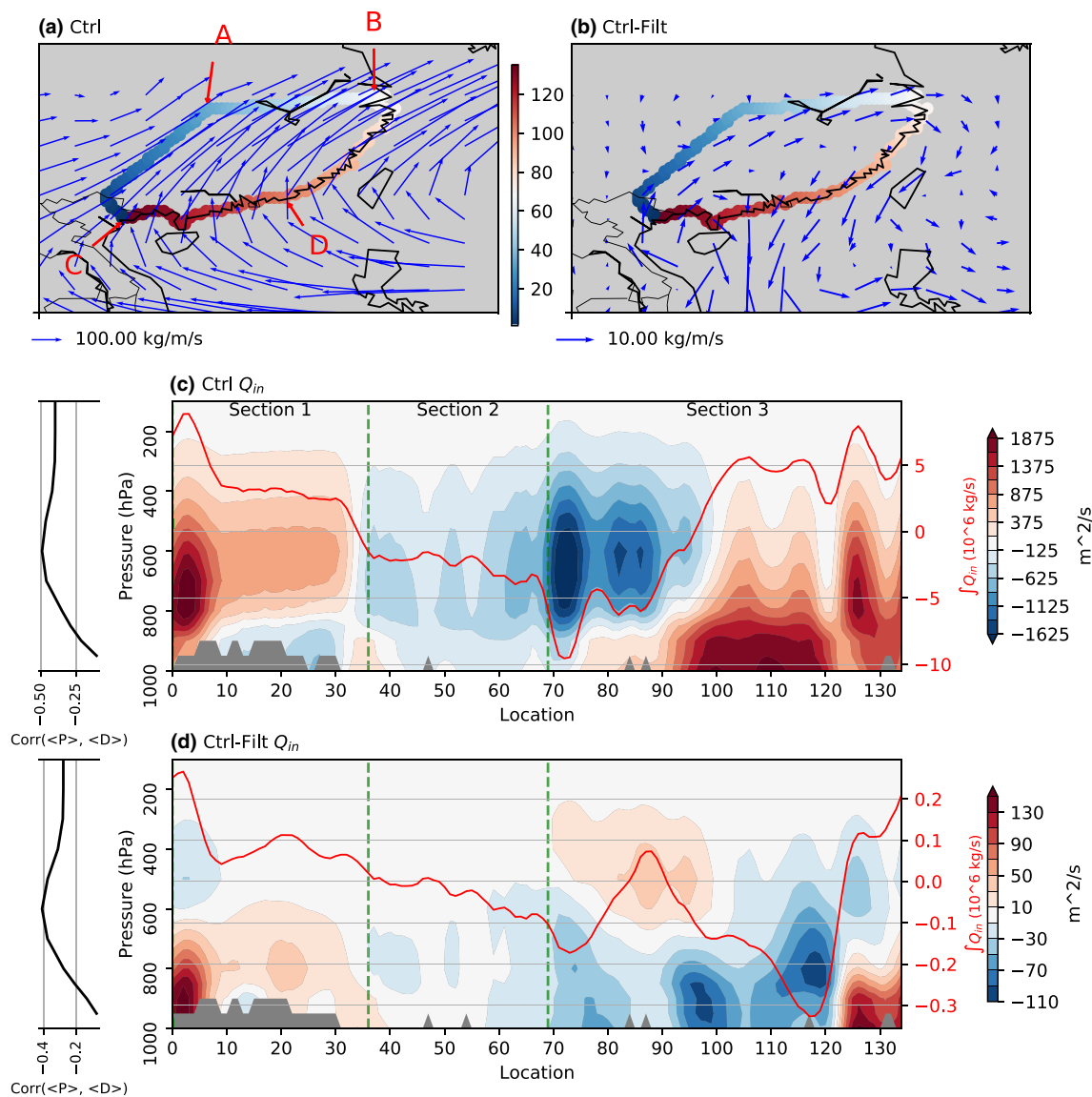


**Fig. 5** **a** The Ctrl average of the vertically integrated moisture fluxes during heavy rainfall days, in kg/m/s. Color pixels denote the boundary cells of SEC, and is divided into Section-1 (*C*A), Section-2 (*A*B) and Section-3 (*B*D*C*). A numerical index is assigned to each boundary cell starting from and finishing at *C*. See the color bar on the right for reference. **b** Similar to **a** but for the Ctrl-Filt differences. **c** A panoramic view of the vertical profile of the cross boundary moisture fluxes into the SEC region in Ctrl ( $uqdy + vqdx$ ), in  $m^2/s$ , averaged during heavy rainfall days. Profile starts from point *C* in **a** and

follows the indices in ascending order, covering Section-1, Section-2 and Section-3 before returning back to *C*. Green dashed lines denote boundaries between Sections 1 and 2, and between Sections 2 and 3. Red curve shows the vertically integrated input flux along the boundary ( $Q_u dy + Q_v dx$ ), in  $10^6$  kg/s, plotted onto the y-axis on the right. Side profile on the left shows the correlation coefficients between SEC precipitation timeseries and that of moisture flux divergences integrated up to different heights. **d** Similar to **c** but for the Ctrl-Filt differences

an entrance between the Taiwan and Hainan islands (Huang et al. 2018a). Given that Section 2 serves mainly as an exit with little net moisture input, Section 3 is the most relevant boundary for receiving oceanic moisture to fuel the SEC precipitation.

Figure 5b, d compare the Ctrl-Filt differences in column integrated moisture fluxes and their vertical distributions during heavy rainfall days. An anomalous offshore flow is found across Section 3 in Ctrl, offsetting the moisture

imports during heavy rainfall events and creating an overall negative convergence anomaly. Vertical profile in Fig. 5d further suggests that this anomaly consists of an upper level input and a lower level output, opposite to the mean state.

Besides quantity, height of moisture import has an important implication on precipitation. Elevated humidity input has restricted vertical lifting space unless strong deep convection is present, which is a requirement difficult to satisfy in this context, given the weak surface heat fluxes at this time

of year, and that cold front systems generally induce vertical turbulences by wedging cold air masses underneath warm air. Furthermore, elevated moisture transport also reduces the chances of topographically induced precipitation.

The side profiles in Fig. 5c, d lend more supports to this argument. Moisture fluxes are integrated in an incremental manner, starting from 1000 hPa up to 100 hPa, with an interval of 100 hPa. At each height, the temporal correlation between SEC precipitation and moisture flux divergence is computed. In both the Ctrl (Fig. 5c) and the Ctrl-Filt difference (Fig. 5d) cases, the strongest (negative) correlation appears around 600 hPa, and weakens as more upper layers are included.

Therefore the upper level moisture input anomaly above  $\sim 600$  hPa in Ctrl is less important to precipitation generation. And the anomalous upper-input-lower-output pattern is suggestive of an anomalous regional overturning circulation that strides across the coasts with a descending branch over SEC, consistent with the enhanced warm-current ascending motion and flanking descending motions discussed previously. In short, horizontal moisture import via the most relevant “gate” is interrupted by this regional overturning circulation, reducing the vapor supply for the land area behind, thus creating a precipitation deficit in Ctrl compared to Filt.

## 4 Conclusion and discussion

A winter SEC precipitation difference is observed in a set of twin WRF simulations with observed and weakened frontal SST forcing. After suppressing meso-scale SSTs with spatial scales less than  $\sim 800$  km, the simulated winter heavy rainfall over SEC was found to be enhanced, giving rise to a moderate yet statistically significant increase in the seasonal average. With the presence of stronger frontal SSTs, moisture transport across the coast was found to be hindered by a regional overturning circulation anchored by the warm Kuroshio current in the nearby ocean, as shown in the schematic diagram in Fig. 6. Anomalous low level

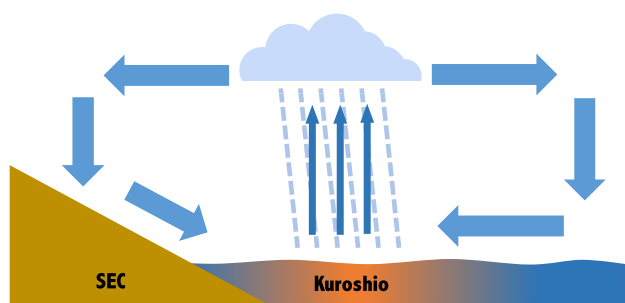


**Fig. 6** Schematic diagram summarizing the effects of frontal SSTs on winter SEC rainfall

wind convergence is found in the warm current front area, triggering convection extending into the free troposphere and generating high precipitation along the warm current. While in the western descending branch of this overturning circulation, anomalous onshore moisture flux is lifted to a higher altitude, before descending to the surface and returning back to ocean, rendering the onshore moisture input less effective for precipitation generation and creating inhibitory downdrafts. In days of heavy rainfall, the anomalous low level returning flow overtakes upper level input flow and drains precipitable water over the land area.

The importance of moisture input orientation and elevation arises when diagnosing the SEC precipitation differences. Moisture budget analysis typically involves quantifying the vertically integrated moisture fluxes and their convergence/divergence. However, the height difference, which has been removed in the vertical integration process, may encode a difference in the relative importance of imported moisture in terms of precipitation generation. In the case of winter SEC heavy rainfall, the coastal boundary is the most important moisture import “gate”, consistent with previous findings (Huang et al. 2018a, b), even though southwesterlies through the western boundary of SEC have comparable magnitudes.

Winter heavy rainfall and moisture fluxes across the land-sea boundary of the SEC coast are associated with atmospheric circulation patterns. During days of heavy precipitation, an anomalous west-low-east-high dipole pressure structure is found in the lower troposphere. As an illustration, Fig. 7a shows a composite of the Ctrl-Filt difference in 850 hPa level geopotential height anomalies ( $Z'_{850}$ ) when the SEC precipitation in Filt exceeds that in Ctrl by  $\geq 3$  mm/day. A relative high is seen over SEC, with a relative low to its east just south of Japan. Besides the relative high over SEC, this regional circulation configuration favours dry and cold northeasterlies in between the positive and negative poles, creating unfavourable conditions for precipitation in Ctrl. The reversed pattern, i.e. a relative low on SEC combined with a relative high to the east, favours the intrusion of relative warm and moist southeasterlies into SEC, leading to more rainfall over the region. In fact, on a day-to-day basis, whichever has notably lower SEC precipitation, whether it being Ctrl or Filt, the composite difference in  $Z'_{850}$  resembles that shown in Fig. 7a, and the negative rainfall anomaly in Ctrl is linked to a significant reduction of heavy rainfall days compared to Filt. Re-examining this relationship backward from pressure differences to precipitation gives consistent results. A Self-Organizing map clustering analysis (Hewitson and Crane 2002, results not shown) was performed on  $Z'_{850}$ , and circulation patterns resemble the dipole structure in Fig. 7a has drier SEC, and vice versa. This relationship is further demonstrated in the correlation patterns in Fig. 7a, between SEC precipitation with  $Z'_{850}$ .

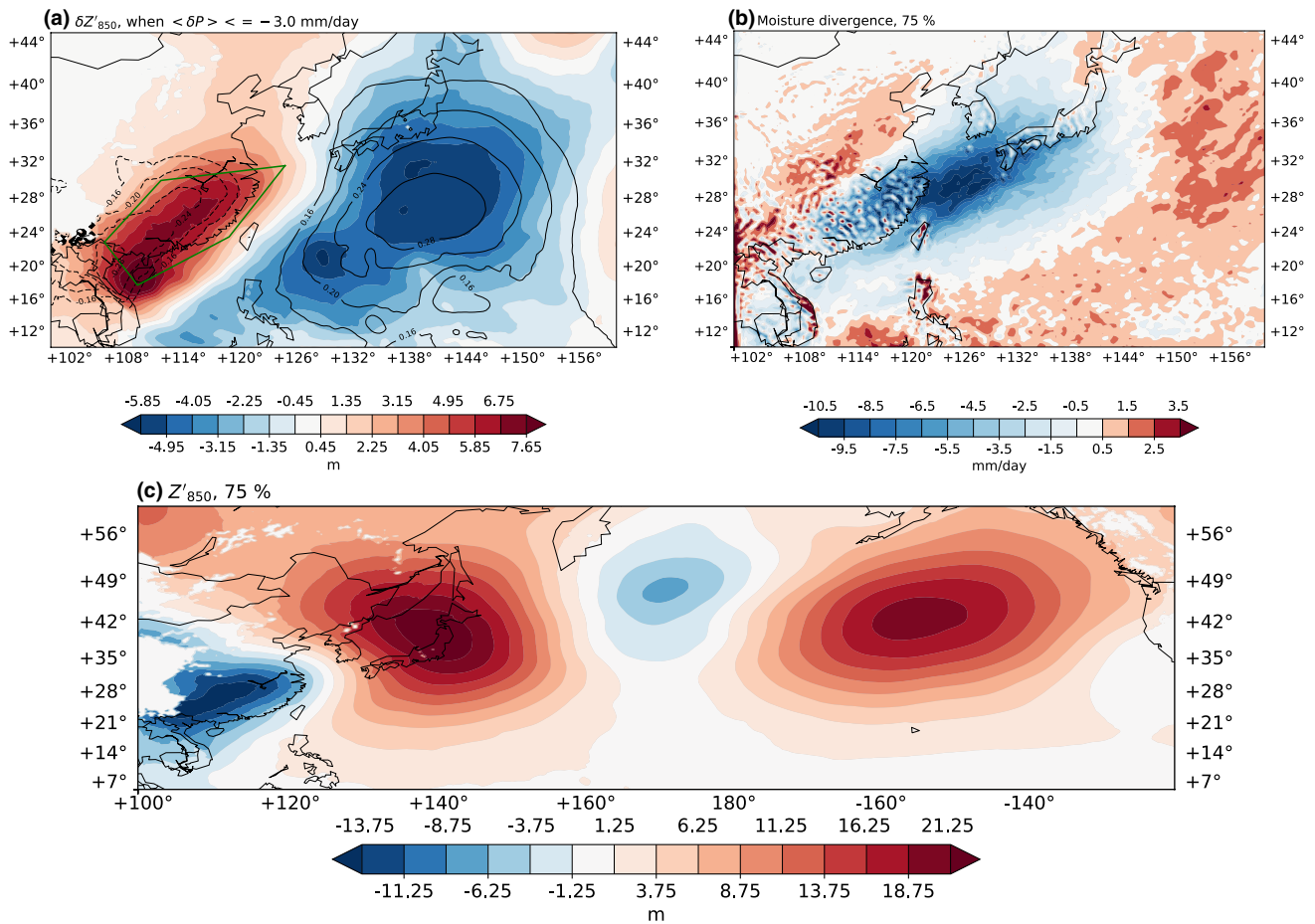


**Fig. 7** **a** Composite of Ctrl-Filt differences in 850 hPa geopotential height anomalies ( $Z'_{850}$ , color, in m) when Ctrl-Filt SEC precipitation difference is below  $-3$  mm/day.  $Z_{850}$  anomalies are defined as deviations from the 13-year annual cycle of Ctrl and Filt combined, smoothed by a 30-day low-pass filter. Superimposed is the correlation coefficients between SEC precipitation and  $Z'_{850}$ , shown in contours

with an interval of 0.04. Only correlations significant at 0.01 level by a Student's t test are shown, and negative values are plotted in dash. **b** Divergence of vertically integrated moisture fluxes in Ctrl averaged during heavy rainfall days, in mm/day. **c** Composite of  $Z'_{850}$  during heavy rainfall days in Ctrl

This pattern may help understand why heavy rainfall in this season tend to show a southwest-northeast diagonal orientation, as shown in Figs. 4b and 7b. In Fig. 7b, surrounding a band of anomalous moisture convergences (a good proxy for enhanced rainfall) extending from SEC to Japan is a ring of anomalous moisture divergences, which may represent the vapor collecting circle. The diagonal convergence band fits into the dipole pressure structure in Fig. 7a.

This dipole pattern has been documented in previous studies and associated with a winter time Rossby wave train (Hu et al. 2017; Huang et al. 2018b). Figure 7c shows the North Pacific sector of this wave train in  $Z'_{850}$  composite during days of heavy rainfall over SEC, with a cyclonic center over SEC and an anticyclonic center to its northeast. The wave pattern is also observed in upper troposphere and in the ERA-I reanalysis dataset (Dee et al. 2011, result not shown). Previously such a wave train has been shown to

originate from the north Atlantic and has close relationship with European blockings (Hu et al. 2017; Huang et al. 2018b), and has been regarded as a triggering mechanism for heavy precipitation over Southeast Asia. However, given the identical boundary conditions in the twin WRF experiments, upstream differences should have been eliminated. Therefore the observed difference in SEC heavy precipitation here raises the possibility of a downstream positive feedback mechanism from the SEC rainfall to the wave train, possibly by an upward transport of latent heat release during heavy rainfall episodes that help maintain the relative vorticity anomaly. Future studies are required to further examine this hypothesis.

Numerical experiment provides an indispensable approach to the study of possible effects of meso-scale SST forcing on the atmosphere, as finding observational evidences can be difficult because of lack of long records of high-resolution

observations. One partial remedy to this difficulty is to compare precipitation changes in ERA-I before and after year 2002. During the period of 1989–2009, ERA-I used a succession of four different SST products as SST forcing (Dee et al. 2011). In particular, the change around 2001–12/2002–01 raised the resolution of SST from  $1.0^\circ \times 1.0^\circ$  to  $0.5^\circ \times 0.5^\circ$ , and from Feb-2009 onward the resolution is further increased to  $0.05^\circ \times 0.05^\circ$  (Parfitt et al. 2017). Given that reanalysis precipitation is model forecast without assimilation, and the close geographical proximity between the cause and effect areas, the before/after 2002 difference may be considered as a *similar* scenario to the Filt-Ctrl comparison in this study. Indeed a winter decrease of SEC rainfall with similar pattern is identified during the decade of 2002–2010 compared with the decade of 1991–2001 (not shown). However, similar decadal difference is also observed in observations from CRUTS3.1 (Harris et al. 2014), GPCCv6 (Becker et al. 2013) and GPCPv2.2 (Adler et al. 2003). Therefore the result from ERA-I is not inconsistent with the mechanism proposed in this study, but also does not prove the proposed the mechanism from an observational perspective.

On the other hand, observations do indicate an accelerated warming along the western boundary warm currents evidenced by winter time oceanic evaporation increases ( $\sim 50$  cm/year between the 1990s and the 1970s, Gimeno et al. 2012), or directly from SST observations on centennial time scale ( $1.29 \pm 0.30$  K over Kuroshio current vs.  $0.62 \pm 0.14$  K for global mean, during 1900–2008, Wu et al. 2012), highlighting the importance of understanding the effect of warm current SST on winter SEC precipitation. Should this hold and the faster warming continues, frontal SST could exert an important impact on regional climate.

**Acknowledgements** This work is supported by the National Key Research and Development Program of China with Grant No. 2017YFC1404000, and a collaborative project between the Ocean University of China (OUC), Texas A&M University (TAMU) and the National Center for Atmospheric Research (NCAR), and by the National Science Foundation of China (NSFC) #41490644 (41490640). We also received support from the NSFC project #41776013. PC acknowledges the supports from NSF AGS-1462127. The Texas Advanced Computing Center at The University of Texas at Austin and the Texas A&M Supercomputing Facility provided high performance computing resources that contributed to the research results. This research is completed through the International Laboratory for High Resolution Earth System Prediction, a collaboration by the Qingdao National Laboratory for Marine Science and Technology Development Center, Texas A&M University, and the National Center for Atmospheric Research. Gratitude is also given to two reviewers who have provided us valuable suggestions.

**Open Access** This article is distributed under the terms of the Creative Commons Attribution 4.0 International License (<http://creativecommons.org/licenses/by/4.0/>), which permits unrestricted use, distribution, and reproduction in any medium, provided you give appropriate credit to the original author(s) and the source, provide a link to the Creative Commons license, and indicate if changes were made.

## References

- Adler RF, Huffman GJ, Chang A, Ferraro R, Xie PP, Janowiak JE, Rudolf B, Schneider U, Curtis S, Bolvin DT, Gruber A, Susskind J, Arkin PPA, Nelkin E (2003) The version-2 global precipitation climatology project (GPCP) monthly precipitation analysis (1979–present). *J Hydrometeorol* 4:1147–1167. [https://doi.org/10.1175/1525-7541\(2003\)004<1147:TVGPCP>2.0.CO;2](https://doi.org/10.1175/1525-7541(2003)004<1147:TVGPCP>2.0.CO;2)
- Annamalai H, Hafner J, Sooraj KP, Pillai P (2013) Global warming shifts the monsoon circulation, drying South Asia. *J Clim* 26:2701–2718. <https://doi.org/10.1175/JCLI-D-12-00208.1>
- Becker A, Finger P, Meyer-Christoffer A, Rudolf B, Schamm K, Schneider U, Ziese M (2013) A description of the global land-surface precipitation data products of the global precipitation climatology centre with sample applications including centennial (trend) analysis from 1901–present. *Earth Syst Sci Data* 5(1):71–99. <https://doi.org/10.5194/essd-5-71-2013>
- Brayshaw DJ, Hoskins BJ, Blackburn M (2008) The storm-track response to idealized sst perturbations in an aquaplanet GCM. *J Atmos Sci* 65:2842–2860. <https://doi.org/10.1175/2008JAS2657.1>
- Cai R, Tan H, Kontoyiannis H (2017) Robust surface warming in off-shore China Seas and its relationship to the East Asian Monsoon wind field and ocean forcing on interdecadal time scales. *J Clim* 30:8987–9005. <https://doi.org/10.1175/JCLI-D-16-0016.1>
- Chelton DB, Schlax MG, Freilich MH, Milliff RF (2004) Satellite measurements reveal persistent small-scale features in ocean winds. *Science* 303:978–983. <https://doi.org/10.1126/science.1091901>
- Compo GP, Kiladis GN, Webster PJ (1999) The horizontal and vertical structure of East Asian winter monsoon pressure surges. *Q J R Meteorol Soc* 125:29–54. <https://doi.org/10.1256/smsqj.55302>
- Dee DP, Uppala SM, Simmons AJ, Berrisford P, Poli P, Kobayashi S, Andrae U, Balmaseda MA, Balsamo G, Bauer P, Bechtold P, Beljaars ACM, van de Berg L, Bidlot J, Bormann N, Delsol C, Dragani R, Fuentes M, Geer AJ, Haimberger L, Healy SB, Hersbach H, Hólmi EV, Isaksen L, Kållberg PW, Köhler M, Matricardi M, McNally AP, Monge-Sanz BM, Morcrette JJ, Park BK, Peubey C, de Rosnay P, Tavolato C, Thépaut JN, Vitart F (2011) The era-interim reanalysis: configuration and performance of the data assimilation system. *Q J R Meteorol Soc* 137:553–597. <https://doi.org/10.1002/qj.828>
- Deng D, Gao S, Du X, Wu W (2012) A diagnostic study of freezing rain over Guizhou, China, in January 2011. *Q J R Meteorol Soc* 138:1233–1244. <https://doi.org/10.1002/qj.981>
- Gimeno L, Stohl A, Trigo RM, Dominguez F, Yoshimura K, Yu L, Drumond A, Durn-Quesada AM, Nieto R (2012) Oceanic and terrestrial sources of continental precipitation. *Rev Geophys* 50:RG4003. <https://doi.org/10.1029/2012RG000389>
- Gonzalez RC, Woods RE (2001) Digital image processing, 2nd edn. Addison-Wesley Longman Publishing Co. Inc., Boston
- Harris I, Jones P, Osborn T, Lister D (2014) Updated high-resolution grids of monthly climatic observations—the cru ts3.10 dataset. *Int J Climatol* 34(3):623–642. <https://doi.org/10.1002/joc.3711>
- Hewitson BC, Crane RG (2002) Self-organizing maps: applications to synoptic climatology. *Clim Res* 22:13–26. <https://doi.org/10.3354/cr022013>
- Hirose N, Ki Fukudome (2006) Monitoring the Tsushima Warm Current improves seasonal prediction of the regional snowfall. *SOLA* 2:61–63. <https://doi.org/10.2151/sola.2006-016>
- Hu K, Huang G, Wu R, Wang L (2017) Structure and dynamics of a wave train along the wintertime Asian jet and its impact on East Asian climate. *Clim Dyn* 51:4123–4137. <https://doi.org/10.1007/s00382-017-3674-1>
- Huang W, He X, Yang Z, Qiu T, Wright JS, Wang B, Lin D (2018a) Moisture sources for wintertime extreme precipitation events over

- South China during 1979–2013. *J Geophys Res Atmos* 123:6690–6712. <https://doi.org/10.1029/2018JD028485>
- Huang W, Yang Z, He X, Lin D, Wang B, Wright JS, Chen R, Ma W, Li F (2018b) A possible mechanism for the occurrence of wintertime extreme precipitation events over South China. *Clim Dyn* 0:1–18. <https://doi.org/10.1007/s00382-018-4262-8>
- Iizuka S (2010) Simulations of wintertime precipitation in the vicinity of Japan: sensitivity to fine-scale distributions of sea surface temperature. *J Geophys Res Atmos* 115(10):1–17. <https://doi.org/10.1029/2009JD012576>
- Jia X, Ge J (2017) Interdecadal changes in the relationship between ENSO, EAWM, and the wintertime precipitation over China at the end of the twentieth century. *J Clim* 30:1923–1937. <https://doi.org/10.1175/JCLI-D-16-0422.1>
- Jia X, Chen L, Ren F, Li C (2011) Impacts of the MJO on winter rainfall and circulation in China. *Adv Atmos Sci* 28:521–533. <https://doi.org/10.1007/s00376-010-9118-z>
- Kanamitsu M, Ebisuzaki W, Woollen J, Yang SK, Hnilo JJ, Fiorino M, Potter GL (2002) Ncep-doe amip-ii reanalysis (r-2). *Bull Am Meteorol Soc* 83:1631–1644. <https://doi.org/10.1175/BAMS-83-11-1631>
- Kobashi F, Xie SP, Iwasaka N, Sakamoto TT (2008) Deep atmospheric response to the North Pacific oceanic subtropical front in spring. *J Clim* 21(22):5960–5975. <https://doi.org/10.1175/2008JCLI2311.1>
- Li XF, Li J, Li Y (2015) Recent winter precipitation increase in the middle-lower Yangtze River Valley since the late 1970s: a response to warming in the Tropical Indian Ocean. *J Clim* 28:3857–3879. <https://doi.org/10.1175/JCLI-D-14-00701.1>
- Li Z, Yang S, He B, Hu C (2016) Intensified springtime deep convection over the South China sea and the Philippine Sea dries Southern China. *Sci Rep* 6:1–9. <https://doi.org/10.1038/srep30470>
- Liang XS (2014) Unraveling the cause-effect relation between time series. *Phys Rev E Stat Nonlinear Soft Matter Phys* 90:052150. <https://doi.org/10.1103/PhysRevE.90.052150>
- Liu JW, Zhang SP, Xie SP (2013) Two types of surface wind response to the East China Sea Kuroshio front. *J Clim* 26(21):8616–8627. <https://doi.org/10.1175/JCLI-D-12-00092.1>
- Liu JW, Xie SP, Yang S, Zhang SP (2016) Low-cloud transitions across the Kuroshio Front in the East China Sea. *J Clim* 29(12):4429–4443. <https://doi.org/10.1175/JCLI-D-15-0589.1>
- Liu X, Chang P, Kurian J, Saravanan R, Lin X (2018) Satellite-observed precipitation response to ocean mesoscale eddies. *J Clim* 31(17):6879–6895. <https://doi.org/10.1175/JCLI-D-17-0668.1>
- Ma X, Chang P, Saravanan R, Montuoro R, Hsieh JS, Wu D, Lin X, Wu L, Jing Z (2015) Distant influence of Kuroshio eddies on North Pacific weather patterns? *Sci Rep* 5:1–7. <https://doi.org/10.1038/srep17785>
- Ma X, Chang P, Saravanan R, Montuoro R, Nakamura H, Wu D, Lin X, Wu L (2017) Importance of resolving Kuroshio front and eddy influence in simulating the North Pacific storm track. *J Clim* 30(5):1861–1880. <https://doi.org/10.1175/JCLI-D-16-0154.1>
- Minobe S, Kuwano-Yoshida A, Komori N, Xie SP, Small RJ (2008) Influence of the Gulf Stream on the troposphere. *Nature* 452:206–209. <https://doi.org/10.1038/nature06690>
- Ogata T, Kitoh A (2014) Effect of high-resolution SST on 60km-AGCM simulated snowfall in Japan. *SOLA* 10:131–135. <https://doi.org/10.2151/sola.2014-027>
- Oort AH, Yienger JJ (1996) Observed interannual variability in the hadley circulation and its connection to ENSO. *J Clim* 9:2751–2767
- Pan J, Yan XH, Zheng Q, Liu WT (2002) Observation of western boundary current atmospheric convergence zones using scatterometer winds. *Geophys Res Lett* 29:13-1. <https://doi.org/10.1029/2002GL015015>
- Parfitt R, Czaja A, Kwon YO (2017) The impact of SST resolution change in the ERA-interim reanalysis on wintertime Gulf Stream frontal air–sea interaction. *Geophys Res Lett* 44:3246–3254. <https://doi.org/10.1002/2017GL073028>
- Ren HL, Ren P (2017) Impact of Madden-Julian oscillation upon winter extreme rainfall in Southern China: observations and predictability in CFSv2. *Atmosphere* 8:192. <https://doi.org/10.3390/atmos8100192>
- Sasaki YN, Yamada Y (2018) Atmospheric response to interannual variability of sea surface temperature front in the East China sea in early summer. *Clim Dyn* 51(7):2509–2522. <https://doi.org/10.1007/s00382-017-4025-y>
- Sasaki YN, Minobe S, Asai T, Inatsu M (2012) Influence of the Kuroshio in the East China sea on the early summer (Baiu) rain. *J Clim* 25(19):6627–6645. <https://doi.org/10.1175/JCLI-D-11-00727.1>
- Sato T, Sugimoto S (2013) A numerical experiment on the influence of the interannual variation of sea surface temperature on terrestrial precipitation in Northern Japan during the cold season. *Water Resour Res* 49(11):7763–7777. <https://doi.org/10.1002/2012WR013206>
- Small RJ, Tomas RA, Bryan FO (2014) Storm track response to ocean fronts in a global high-resolution climate model. *Clim Dyn* 43:805–828. <https://doi.org/10.1007/s00382-013-1980-9>
- Trenberth KE (1984) Some effects of finite sample size and persistence on meteorological statistics. Part I: autocorrelations. *Mon Weather Rev* 112(12):2359–2368. [https://doi.org/10.1175/1520-0493\(1984\)112<2359:SEOFSS>2.0.CO;2](https://doi.org/10.1175/1520-0493(1984)112<2359:SEOFSS>2.0.CO;2)
- Trenberth KE, Dai A, Rasmussen RM, Parsons DB (2003) The changing character of precipitation. *Bull Am Meteorol Soc* 84:1205–1217. <https://doi.org/10.1175/BAMS-84-9-1205>
- Trenberth KE, Smith L, Qian T, Dai A, Fasullo JT (2007) Estimates of the global water budget and its annual cycle using observational and model data. *J Hydrometeorol* 8:758–769. <https://doi.org/10.1175/JHM600.1>
- Tropical Rainfall Measuring Mission (TRMM) (2011) TRMM (TMPA) rainfall estimate L3 3 hour 0.25 degree x 0.25 degree V7. Goddard Earth Sciences Data and Information Services Center (GES DISC) <https://doi.org/10.5067/TRMM/TMPA/3H/7>
- Wan RJ, Wu GX (2007) Mechanism of the spring persistent rains over southeastern China. *Sci China Ser D Earth Sci* 50:130–144. <https://doi.org/10.1007/s11430-007-2069-2>
- Wang B, Wu R, Xiouhua F (2000) Pacific–East Asian teleconnection: how does ENSO affect East Asian Climate?\*. *J Clim* 13:1517–1536. [https://doi.org/10.1175/1520-0442\(2000\)013<1517:PEATHD>2.0.CO;2](https://doi.org/10.1175/1520-0442(2000)013<1517:PEATHD>2.0.CO;2)
- Wilks DS (2011) On the reliability of the rank histogram. *Mon Weather Rev* 139:311–316. <https://doi.org/10.1175/2010MWR3446.1>
- Wu MC, Chan JCL (1997) Upper-level features associated with winter monsoon surges over South China. *Mon Weather Rev* 125:317–340. [https://doi.org/10.1175/1520-0493\(1997\)125<0317:ULFAWV>2.0.CO;2](https://doi.org/10.1175/1520-0493(1997)125<0317:ULFAWV>2.0.CO;2)
- Wu R, Hu ZZ, Kirtman BP (2003) Evolution of ENSO-related rainfall anomalies in East Asia. *J Clim* 16(22):3742–3758. [https://doi.org/10.1175/1520-0442\(2003\)016<3742:EOERA1>2.0.CO;2](https://doi.org/10.1175/1520-0442(2003)016<3742:EOERA1>2.0.CO;2)
- Wu L, Cai W, Zhang L, Nakamura H, Timmermann A, Joyce T, McPhaden MJ, Alexander M, Qiu B, Visbeck M, Chang P, Giese B (2012) Enhanced warming over the global subtropical western boundary currents. *Nat Clim Change* 2:161–166. <https://doi.org/10.1038/nclimate1353>
- Xie SP (2004) Satellite observations of cool ocean–atmosphere interaction. *Bull Am Meteorol Soc* 85(2):195–208. <https://doi.org/10.1175/BAMS-85-2-195>
- Xie SP, Hafner J, Tanimoto Y, Liu WT, Tokinaga H, Xu H (2002) Bathymetric effect on the winter sea surface temperature and climate of the yellow and East China seas. *Geophys Res Lett* 29(24):81-1–81-4. <https://doi.org/10.1029/2002GL015884>

- Xie W, Li N, Li C, Wu Jd, Hu A, Hao X (2014) Quantifying cascading effects triggered by disrupted transportation due to the great 2008 Chinese ice storm: implications for disaster risk management. *Nat Hazards* 70:337–352. <https://doi.org/10.1007/s11069-013-0813-9>
- Xu H, Xu M, Xie SP, Wang Y (2011) Deep atmospheric response to the spring Kuroshio over the East China sea. *J Clim* 24(18):4959–4972. <https://doi.org/10.1175/JCLI-D-10-05034.1>
- Yao Y, Lin H, Wu Q (2015) Subseasonal variability of precipitation in China during boreal winter. *J Clim* 28:6548–6559. <https://doi.org/10.1175/JCLI-D-15-0033.1>
- Ye Q (2014) Building resilient power grids from integrated risk governance perspective: a lesson learned from China's 2008 ice-snow storm disaster. *Eur Phys J Spec Top* 223:2439–2449. <https://doi.org/10.1140/epjst/e2014-02218-7>
- Zhou LT (2011) Impact of East Asian winter monsoon on rainfall over Southeastern China and its dynamical process. *Int J Climatol* 31:677–686. <https://doi.org/10.1002/joc.2101>
- Zhou LT, Wu R (2010) Respective impacts of the East Asian winter monsoon and ENSO on winter rainfall in China. *J Geophys Res Atmos* 115:1–11. <https://doi.org/10.1029/2009JD012502>
- Zhou B, Gu L, Ding Y, Shao L, Wu Z, Yang X, Li C, Li Z, Wang X, Cao Y, Zeng B, Yu M, Wang M, Wang S, Sun H, Duan A, An Y, Wang X, Kong W (2011) The great 2008 Chinese ice storm its socioeconomic-ecological impact and sustainability lessons learned. *Bull Am Meteorol Soc* 92:47–60. <https://doi.org/10.1175/2010BAMS2857.1>
- Zhou MG, Wang LJ, Liu T, Zhang YH, Lin HL, Luo Y, Xiao JP, Zeng WL, Zhang YW, Wang XF, Gu X, Rutherford S, Chu C, Ma WJ (2014) Health impact of the 2008 cold spell on mortality in subtropical China: the climate and health impact national assessment study (CHINAs). *Environ Health* 13:60. <https://doi.org/10.1186/1476-069X-13-60>
- Zhou B, Wang X, Cao Y, Ge X, Gu L, Meng J (2017) Damage assessment to subtropical forests following the 2008 Chinese ice storm. *IForest* 10:406–415. <https://doi.org/10.3832/ifor1619-009>

**Publisher's Note** Springer Nature remains neutral with regard to jurisdictional claims in published maps and institutional affiliations.